

CrossMark  
click for updatesCite this: *Energy Environ. Sci.*,  
2016, 9, 663Received 7th November 2015,  
Accepted 18th December 2015

DOI: 10.1039/c5ee03404c

www.rsc.org/ees

## A flexible solid-state electrolyte for wide-scale integration of rechargeable zinc–air batteries†

Jing Fu,<sup>a</sup> Jing Zhang,<sup>a</sup> Xueping Song,<sup>b</sup> Hadis Zarrin,<sup>a</sup> Xiaofei Tian,<sup>b</sup> Jinli Qiao,<sup>c</sup> Lathanken Rasen,<sup>a</sup> Kecheng Li<sup>b</sup> and Zhongwei Chen<sup>\*a</sup>

Rechargeable zinc–air batteries, having high energy densities and cost-effectiveness, are important environmentally-benign energy storage solutions. Here we developed a facile strategy for fabricating a nanoporous alkaline-exchange electrolyte membrane from natural cellulose nanofibres, exhibiting high ionic-conductivity and water retention as well as high bending flexibility. These advantages render the membrane a promising solid-state electrolyte for rechargeable zinc–air batteries in lightweight and flexible electronic applications.

### Broader context

Technological improvement that enables batteries with high energy-density, flexibility and safety is being driven by an ever-increasing demand for many new applications. From portable electronics to electric vehicles, rechargeable zinc–air batteries hold great promise as environmentally-benign, reliable, and high-energy-density devices. Zinc–air batteries owe the superior energy density from their unique “half-open” system where the active material (oxygen) undergoing the redox reaction is obtained directly from the atmosphere. However, in portable applications their merits are largely limited by their bulky battery configurations mainly relying on liquid electrolytes. One approach to overcome this barrier is to replace the incumbent liquid electrolytes with versatile, solid-state alternatives in rechargeable zinc–air batteries. Here we developed a porous alkaline-exchange electrolyte membrane based on functionalized cellulose nanofibers for solid-state rechargeable zinc–air batteries, exhibiting high hydroxide-ion conductivity and water retention as well as high flexibility. Without the packaging limitation of liquid electrolytes, a thin-film zinc–air battery employed with our functionalized cellulose membrane can be made into versatile shapes, allowing for easy integration of rechargeable zinc–air into any bendable and wearable devices.

## Introduction

Conventional batteries tend to be bulky and heavy relative to the amount of energy they store, they thus pose challenges for specific applications particularly in portable electronics with arbitrary shapes. Therefore, future development of battery technologies is moving toward thin, flexible and high-energy-density solutions.<sup>1–4</sup> Compared to batteries with closed systems such as lithium-ion, zinc–air batteries possess an unique half-closed system that uses the oxygen reactant at their air electrodes.<sup>5</sup> This feature results in a high theoretical energy density associated with zinc–air batteries, making them a promising solution in flexible energy storage devices.<sup>6,7</sup> Additionally, zinc–air

batteries are relatively inexpensive to produce and safe to operate.<sup>8,9</sup> However, the majority of zinc–air battery technologies to date has utilized aqueous alkaline electrolytes, which are not suitable for integrating into flexible devices.<sup>10–14</sup> In order to realize their flexible applications, transitioning from aqueous electrolytes to shape-conformable solid-state electrolytes is of primary importance. The solid-state electrolytes can function as both aqueous electrolytes providing ion conduction and separators preventing the battery internal short-circuiting, thus greatly simplifying the design and fabrication process of the batteries. There are commonly two approaches for fabricating solid-state electrolytes.<sup>15</sup> One is to impregnate basic (OH<sup>−</sup>) functional groups into polymer backbone with a single phase (*i.e.*, alkaline anion-exchange membranes, AAEM), and the other is to incorporate alkaline salts into inert polymer matrix (*i.e.*, gel electrolyte membranes). AAEM have been widely applied to alkaline fuel cell applications.<sup>16–19</sup> They also show a great promise in zinc–air batteries, in which they conduct hydroxide ions during battery operations and prevent zinc ion migration from reaching the air electrode. However, their ionic conductivities, which strongly rely on the ion-exchange capacities and degree of hydration,

<sup>a</sup> Department of Chemical Engineering, Waterloo Institute for Nanotechnology, Waterloo Institute for Sustainable Energy, University of Waterloo, Waterloo, Ontario N2L 3G1, Canada. E-mail: zhwen@uwaterloo.ca

<sup>b</sup> Department of Chemical Engineering, University of New Brunswick, Fredericton, New Brunswick, E3B 5A3, Canada

<sup>c</sup> College of Environmental Science and Engineering, Donghua University, Shanghai 201620, P. R. China

† Electronic supplementary information (ESI) available. See DOI: 10.1039/c5ee03404c

are very limited to boost power and energy performance of zinc–air batteries. In addition, the water retaining property of AAEM is relatively poor. As a result, the membranes tend to lose water rapidly by evaporation because the air electrodes are exposed to the atmosphere, thus leading to a fast degradation of their ionic conductivities and the resultant battery performance. On the contrary, gel electrolyte membranes exhibit good electrolyte absorbing capabilities, functioning as electrolyte reservoirs. This property leads to a high hydroxide-ion capacity of the gelled membranes, and thus facilitating the hydroxide-ion conduction and kinetic reactions of zinc–air batteries. Unfortunately, they can hardly provide sufficient physical protection between the electrodes compared to AAEM or commercially available separators (*i.e.* Celgard<sup>®</sup>) due to their high hydrophilicity and the resulting relatively poor dimensional stability. More importantly, another issue associated with gel electrolyte membranes is their progressive release of the doped alkali. This alkali loss will cause a large ohmic polarization of the zinc–air batteries, which severely damages the batteries' power and energy performance.

To address these challenges, we developed a green, efficient and easy-to-scale-up strategy for fabricating a thin, ultra-flexible and hydroxide (OH<sup>−</sup>) conductive, nanofibrous cellulose electrolyte membrane with high water retention for zinc–air battery applications. Being the most earth-abundant, renewable polymer material on the earth, natural cellulose fibres play a critically important role in addressing future energy and environmental challenges.<sup>20–26</sup> The cellulose nanofibres are particularly interesting due to their appealing characteristics, such as large specific surface area rich in hydroxyl groups, high mechanical strengths, high surface-to-volume ratios and lightweight,<sup>27–29</sup> offering the possibility of being solid-state electrolytes for lightweight and flexible energy storage devices. Here, the developed approach takes the advantage of these unique properties of cellulose nanofibres, so that a thin and robust nanofibrous membrane with high water retention can be achieved. Meanwhile, hydroxide-ion conductive cellulose nanofibres are designed through a surface-functionalization of these nanofibres. Particularly, a self-crosslinking occurs among these functionalized nanofibers at mild temperature (60 °C), which can further enhance the dimensional stability of the membrane. The promise by enhancing the intrinsic physical and chemical properties of cellulose nanofibers leads to appreciable improvements in both the mechanical integrity and hydroxide ion conductivity of the nanofibrous membrane for the use in zinc–air batteries.

## Experimental

### Preparation of cellulose nanofibers

The cellulose nanofibres were produced from Northern Bleached Softwood Kraft pulp (New Brunswick, Canada) through pre-refining, enzymatic processing and nano-refining. The disintegrated pulp was pre-refined using Noram PFI mill (Quebec, Canada) with a revolution of 30 000. To gain a uniform pulp suspension, an enzyme treatment of the refined pulp was conducted by using a mixture of two enzymes (*i.e.*, Mannanase and Xylanase) from Novozymes (Franklinton, USA). The enzyme treated pulp was thoroughly

washed with DDI water to remove any soluble residues and was charged into the PFI mill with the revolution up to 30 000 to produce cellulose micro/nanofibrils.

### Fabrication of hydroxide-conductive nanoporous cellulose membrane

Dimethyloctadecyl[3-(trimethoxysilyl)propyl]ammonium chloride (DMOAP) (42 wt% in methanol, Sigma Aldrich) was used as the precursor for functionalizing cellulose nanofibers. First, the cellulose nanofibres were dispersed and stirred in DDI water to get a uniform cellulose fiber suspension. DMOAP precursor was diluted with methanol solution to a concentration of 10% and then was added into the cellulose fibre suspension. The amount of DMOAP varied from 100 to 300 mol% with respect to the cellulose repeating glucose unit. The mixture of cellulose fibres and DMOAP was stirred at room temperature for 12 h. Then, the resulting solution was centrifuged and washed several times with ethanol and DDI water to remove any unreacted traces of DMOAP. The quaternary ammonium functionalized cellulose membrane was fabricated by vacuum filtration and dried at room temperature for 6 h and then was cross linked at 60 °C under vacuum for another 24 h. The resulting membrane with a thickness of 30 μm was hydroxide-exchanged from Cl<sup>−</sup> form to OH<sup>−</sup> form in 1 M KOH solution for 24 h. Finally, the hydroxide-exchanged membrane was washed and soaked in DDI water. The 1 M KOH-doped pristine cellulose (KOH-PC) membrane was prepared by soaking the pristine cellulose membrane in 1 M KOH solution for 24 h without washing by DDI water.

### Fabrication of solid-state rechargeable zinc–air battery

A flexible zinc electrode, consisted of zinc powder (purity powder, Sigma Aldrich), carbon nanofiber, carbon black and poly(vinylidene fluoride-co-hexafluoropropene) polymer binder,<sup>6</sup> was prepared for the battery testing. The mass of the zinc electrode as prepared was 40 mg. The as-received Co<sub>3</sub>O<sub>4</sub> nanoparticles (<50 nm particle size, Sigma Aldrich) was used as the bi-functional electroactive material to fabricate the air electrode. Catalyst ink consisted of Co<sub>3</sub>O<sub>4</sub>, ionomer (AS-4, Tokuyama Inc.) and 1-propanol was sprayed onto a carbon cloth (Fuel Cell Technology) as the gas diffusion layer with a catalyst loading of 1.0 mg cm<sup>−2</sup>. The in-house battery prototype was fabricated through a layer-by-layer method by which the electrodes were placed face-to-face with the membrane. All the tested membranes were pre-wetted by 1 M KOH solution before the battery assembly.

### Characterization and electrochemical measurements

X-Ray Diffraction (XRD) (INEL XRG 3000), Fourier transform infrared spectra (FTIR) (Avatar 320) and X-ray photoelectron spectroscopy (XPS) (Thermo Scientific Al K-Alpha X-ray source) were conducted to characterize crystal structure and the surface chemistry of the functionalized cellulose membranes. Scanning electron microscopy (SEM) (LEO FESEM 1530) and transmission electron microscopy (TEM) (Bruker AXS D8 Advance) were utilized to observe the morphology of the cellulose nanofibers and the membrane. Pore size distribution of the membrane was characterized by atomic force microscope (AFM) (Veeco Dimension 3000).

Electrochemical impedance spectroscopy (EIS) (VersaSTAT MC potentiostat) was carried out in the frequency ranging from 100 kHz to 0.05 Hz with potential amplitude of 20 mV. The battery electrochemical evaluation was conducted under atmospheric air. Polarization data was collected using galvanodynamic method at a scan rate of 1.0 mA s<sup>-1</sup> with cut-off voltage of 0.5 V for the discharge and 2.5 V for the charge. Galvanostatic discharge was tested at various constant current densities using a battery tester (Neware BTS3000). Discharge and charge cycling was conducted by a recurrent galvanic pulse method at a constant current density of 250 mA g<sup>-1</sup> with each cycle consisting of 30 min for discharge followed by 30 min charge.

## Results and discussion

### Structural and morphological characterization

The quaternary ammonia-functionalized nanocellulose (QAFC) membrane was fabricated through a filtration process (Fig. S1a, ESI†). This filtration of water-based, functionalized cellulose fibre suspension is considered to be a reliable, low-cost and scalable process to fabricate the membrane. The QAFC membrane contains numerous cellulose fibres including micron-sized fibre bundles and micro/nanofibrils, which result in a translucent membrane (Fig. 1a). The structure of a solid-state rechargeable zinc–air battery using the QAFC membrane was also illustrated in Fig. 1a. During the discharge, the generated hydroxide ions can migrate from the reaction site of the air electrode to the zinc electrode forming zinc oxide. While charging, the QAFC membrane can transport the hydroxide ions produced at the zinc electrode to the air electrode, at which the oxygen evolution reaction takes place. The surface changes in chemical structure of the functionalized cellulose nanofibers are illustrated in Fig. 1b. Dimethyloctadecyl[3-(trimethoxysilyl)propyl]ammonium chloride (DMOAP) was utilized as the functional precursor containing quaternary ammonia (QA) moieties. First, DMOAP initiated the quaternarization of cellulose nanofibers (Fig. 1b,

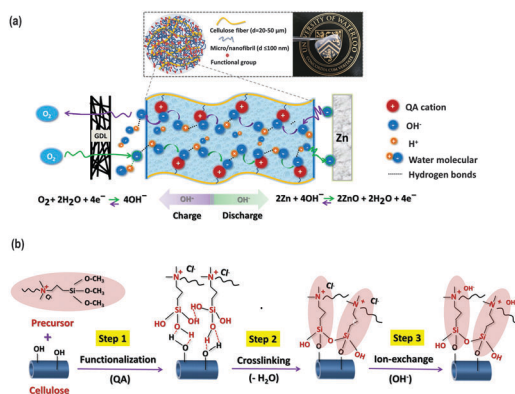


Fig. 1 (a) Schematic diagram of the solid-state rechargeable zinc–air battery using the functionalized nanocellulose membrane. (GDL: gas diffusion layer; QA: quaternary ammonium) (b) The chemical structure evolution of the cellulose nanofibre surface after functionalization, cross-linking and hydroxide-exchange.

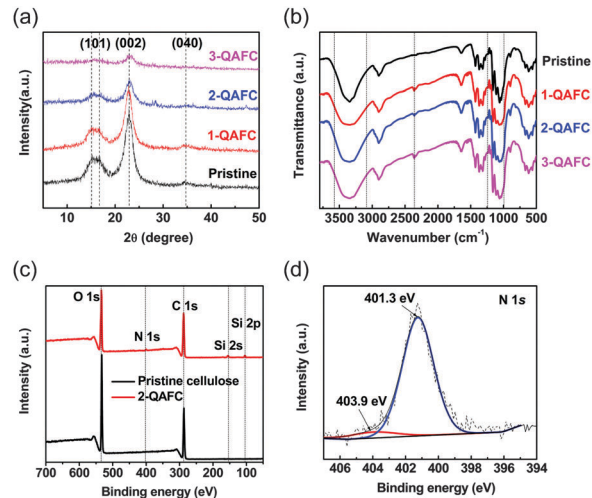


Fig. 2 (a) X-ray diffraction and (b) FT-IR spectra of the PC and QAFC membranes. (c) XPS survey spectra of the PC and 2-QAFC membranes, and (d) deconvolution of N 1s peak of the 2-QAFC membrane.

step 1) through the formation of hydrolyzed silanol intermediates and the adsorption of these intermediates onto the cellulose surface by hydrogen bonding (Fig. S1b, ESI†).<sup>30</sup> Subsequent thermal treatment, namely, crosslinking process (Fig. 1b, step 2), allowed these hydrolyzed functional moieties further to react with the hydroxyl groups of the cellulose by forming the interfacial covalent bonds (Si–O–C). Additionally, the hydroxyl groups of the functional moieties can undergo self-crosslinking and form siloxane bonds (Si–O–Si). As a result, a covalent cross-linking bonding-network (Fig. S1c, ESI†), formed between the functional moieties and the cellulose nanofibres, is considered to enhance the dimensional stability of the membrane.<sup>31–33</sup> The functional groups as attached were further alkaline exchanged (Fig. 1b, step 3) and thus the membrane became hydroxide (OH<sup>-</sup>) conductive.

The crystalline structure of the membrane made of the pristine cellulose nanofibres (PC membrane) and QAFC membranes were studied by XRD (Fig. 2a). The cellulose nanofibres modified with 100 mol%, 200 mol% and 300 mol% concentration of DMOAP are denoted as 1-QAFC, 2-QAFC and 3-QAFC, respectively. The PC membrane displayed a typical profile of cellulose I crystalline form with three characteristic peaks corresponding to crystalline planes (101), (002) and (040).<sup>34</sup> However, strong reductions of all the three characteristic peaks for the QAFC membranes were detected after the functionalization. Specifically, with an increased concentration of DMOAP in the reaction, more pronounced decreases at the (002) plane were observed for the 2-QAFC and 3-QAFC samples, indicating that a significant portion of the cellulose I crystalline structure had transformed into the amorphous phase. This result suggests that the flexibility of cellulose nanofibers can be improved after the functionalization, which is due probably to the increase of the amorphous regions in the QAFC membranes. Moreover, the local hydrophilic domain near the hydroxide-ion charges will increase accordingly with the increased amorphousness in the membrane, making ion transport will become easier through these hydrated regions.<sup>35</sup>

FT-IR spectra of the PC membrane and QAFC membranes are compared in Fig. 2b. The peak at  $\sim 3360\text{ cm}^{-1}$  corresponds to the O–H stretch vibration of intramolecular and intermolecular hydrogen bonds in the PC membrane. The fact that the peak tended to broaden for the QAFC membranes in the region  $3480\text{--}3220\text{ cm}^{-1}$  could be associated with a large quantity of absorbed water in the more amorphous domain in the QAFC membranes.<sup>36</sup> Additionally, the increase in the absorption intensity at  $1640\text{ cm}^{-1}$ , assigned to the water bending vibration in the amorphous regions, implies a higher amount of the bound water in the QAFC membranes.<sup>37</sup> The new peaks at  $\sim 2350\text{ cm}^{-1}$ , assigned to the O=C=O stretching vibration mode, are correlated with the carbonate species formed in the QAFC membranes. The presence of carbonate species is due to the dissociated hydroxide ions in the QAFC membranes that can be converted into carbonates by the adsorption of  $\text{CO}_2$  from the air.<sup>38</sup> Particularly, this peak intensity increased accordingly with increasing the concentration of DMOAP in the reaction; a trend which is consistent with the degree of QA functionalization. Additionally, although there is an overlap of Si–O–Si, Si–O–C and C–O stretching in the band region of  $1000\text{--}1250\text{ cm}^{-1}$  in the PC and QAFC membranes,<sup>39</sup> the intensity of the broad peak at  $1055\text{ cm}^{-1}$  (Si–O–Si) increased with the degree of QA functionalization, confirming the successful functionalization of cellulose nanofibers. XPS was carried out to further investigate the changes in surface chemistry resulting from the functionalization of cellulose nanofibers. The XPS survey spectra of the PC and 2-QAFC membranes are displayed in Fig. 2c. Compared to the O/C atomic ratio of the PC membrane (0.69), the value of the 2-QAFC membrane decreased toward 0.51, indicative of a relative increase in carbon atoms at the cellulose surface due to the long alkyl chains of the attached QA functional groups. Three new peaks of the 2-QAFC membrane at binding energies of 103.1 eV, 154.1 eV and 401.4 eV are assigned to Si 2p, Si 2s and N 1s, respectively, whereas the presence of N and Si is not detected in the PC membrane. Additionally, the nitrogen bonding states of the 2-QAFC membrane are distinctive from high-resolution N 1s spectrum in Fig. 2d. The strong peak at 401.3 eV (92.9 atomic%) was attributed to quaternary-N species in 2-QAFC,<sup>40</sup> while the small peak at 403.9 eV (7.1 atomic%) was related to quaternary-N<sup>+</sup>–O<sup>–</sup> species.<sup>32</sup> The result reveals that quaternary ammonium was the dominant nitrogen species in the 2-QAFC membrane.

The as-prepared cellulose nanofibers are composed of a variety of micron-sized cellulose fibres and fine fibrils with lengths of over several hundred microns (Fig. 3a). Fig. 3b exhibits that the fine fibrils unravelled from the micron-sized fibre fragment have a greatly expanded surface area. TEM images (Fig. 3c and d) further identify that the diameters of these fine fibrils range from 10–30 nm for nanofibrils up to several hundred nanometers for microfibrils. These isolate nanofibers (micro/nanofibrils) tend to construct smaller porous structure with a higher surface area in the fibrous membrane than the micron-sized fibres. The surface morphology of the 2-QAFC membrane was further characterized by SEM. The membrane surface appears as a homogenous and dense nanofiber network intertwined with the micron-sized fibres functioning as the strong “scaffold” (Fig. 3e). A high resolution

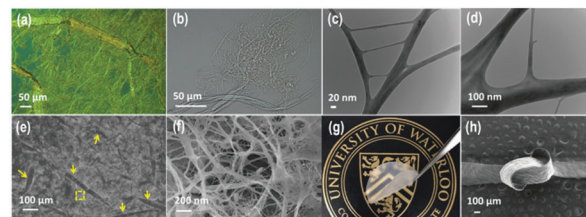


Fig. 3 (a) and (b) Optical images of the cellulose fibre bundles with unravelled fine fibrils. (c) and (d) TEM images of the micro/nanofibrils. (e) A SEM image (surface view) of the 2-QAFC membrane. Yellow arrows point to the micron-sized cellulose fibre bundles. (f) A high magnification SEM image from the square region of (e) outlined in yellow. (g) A photograph of the 2-QAFC membrane having a translucent appearance. (h) A SEM image of a knotted 2-QAFC membrane showing excellent flexibility.

SEM image (Fig. 3f) reveals that the membrane possesses a porous structure in the nanoscale with a significant amount of pores throughout the nanofiber network. Further, the high resolution scanning allowed visualization of pores and determination of pore size distributions (Fig. S2, ESI<sup>†</sup>). The pore size ranges from 25–300 nm, and the porosity is determined to be 72.8%. The nanosized pores and nanofibres in the membrane are smaller than the wavelengths of visible lights, making the membrane translucent (Fig. 3g).<sup>41</sup> In addition, the large contact area and covalent cross-linking bonds among functionalized nanofibres within the nanofiber network, along with the high strength of individual nanofibres give the membrane a very strong mechanical property.<sup>42</sup> A microscopic view of a knotted 2-QAFC membrane in Fig. 3h reveals its excellent flexibility without discernible physical fracture.

### Water uptake and swelling behaviour

In addition to the outstanding flexibility, the interconnected nanoporous structure of the 2-QAFC membrane plays an important role in absorbing and retaining water as well as maintaining dimensional stability in the water-swollen state of the membrane. It is apparent that high water uptake would be favourable for ionic conductivity, benefiting from the hydrated ion-transport channels throughout the membrane.<sup>35</sup> For the purpose of comparison, the water uptake and swelling behaviour of the commercial AAEM (A201, Tokuyama Corporation, Japan), 2-QAFC and PC membranes were measured (Table 1). The PC membrane showed more than 2 times higher water uptake than that of the A201 membrane, owing to the excellent hydrophilic nature of cellulose and the large internal surface area of cellulose nanofibres within the nanoporous structure. Compared to the PC membrane, the 2-QAFC membrane showed a slightly higher water uptake but a pronounced lower through-plane and in-plane swelling ratios. The result suggests that the covalent cross-linking bonding-network (Fig. S1c, ESI<sup>†</sup>) formed between the functionalized cellulose nanofibres in the 2-QAFC membrane is strong enough to allow the membrane to hold a significant amount of water with lower bulk volume expansion.<sup>41</sup> The ratio of through-plane swelling to in-plane swelling is often used to depict the extent of swelling anisotropy of membranes.<sup>43</sup> Compared to the A201 membrane, the fully hydrated PC membrane exhibited a much

Table 1 Physical properties of the PC, 2-QAFC and A201 membranes

Membrane	PC	2-QAFC	A201
Thickness ( $\mu\text{m}$ )	30	30	28
Water uptake (%)	95.4	95.6	44.3
In-plane swelling ratio (%)	17.8	13.6	8.2
Through-plane swelling ratio (%)	50.2	14.6	35.7
Anisotropic swelling degree	2.8	1.1	4.4

lower anisotropic swelling degree (Table 1). In addition, this anisotropic swelling behaviour is even less affected by the functionalization. It was found that the 2-QAFC membrane showed only moderate anisotropic swelling as its anisotropy degree (1.1) was even lower than that of the PC membrane (2.8). This result demonstrates that the surface-functionalization of cellulose nanofibers enhances the dimensional integrity of the membrane by decreasing the swelling of both the in-plane and through-plane direction. The strong dimension integrity of the membrane is particularly desirable for long-term battery cycling operation.

### Electrochemical characterization and performance

**Ionic conductivity.** The ionic conductivities ( $\sigma$ ) of the PC and QAFC membranes were measured using a four-probe alternating current (AC) impedance spectroscopy method. As shown in Fig. 4a, the ionic conductivities of the QAFC membranes were significantly improved compared to that of the PC membrane. The marked improvement in the ionic conductivity is ascribed to the hydroxide ions disassociated from the QA functional groups in the hydrated regions. It also should be noted that the chemical and nanoporous structure of the QAFC membranes can trap extra alkali during the hydroxide exchange process. The excess “free” (physically absorbed and hydrogen bonded) alkali will result in an improvement of the ionic conductivity.<sup>44–46</sup> Fig. S3 (ESI<sup>†</sup>) shows the ionic conductivity of the 2-QAFC membrane soaked in DDI water as a function of time. While a decline in conductivity was observed at an initial stage, the conductivity of the 2-QAFC membrane did not show further decrease after 80 h. The initial decrease of the conductivity is mainly due to the excess “free” alkali which was gradually leached out in water. Regardless of the release of alkali, the 2-QAFC membrane exhibited a high ionic conductivity of  $21.2 \text{ mS cm}^{-1}$ , benefiting from the dissociated hydroxide ions from QA functional groups in the membrane. To better understand the ion transport mechanism of the 2-QAFC membrane, the temperature dependence of the ionic conductivity was evaluated in the range of  $30 \text{ }^\circ\text{C}$  to  $70 \text{ }^\circ\text{C}$ . The commercial A201 membrane was also plotted for comparison. As shown in Fig. 4b, the 2-QAFC membrane exhibited a similar positive temperature-conductivity linear relationship to the A201 membrane, indicating the transport of hydroxide charge ( $\text{OH}^-$ ) in the 2-QAFC membrane results from the Grotthuss hopping mechanism.<sup>47,48</sup> The activation energies ( $E_a$ ) can be evaluated from the slope of the  $\ln(\sigma)$  vs.  $(1000/T)$  using the Arrhenius equation. The  $E_a$  of the A201 membrane is  $11.26 \text{ kJ mol}^{-1}$ , in agreement with that reported in the literature,<sup>48</sup> whereas the  $E_a$  of the 2-QAFC membrane ( $8.76 \text{ kJ mol}^{-1}$ ) is considerably smaller

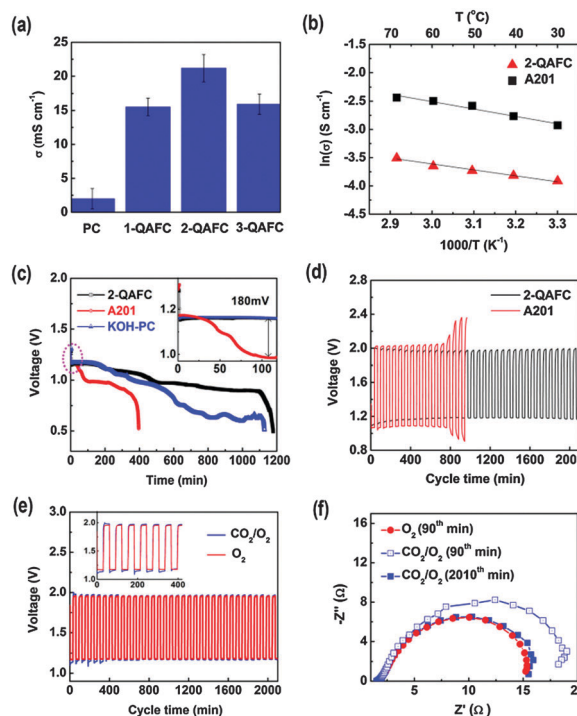


Fig. 4 (a) Ionic conductivity of the PC and QAFC membranes. (b) Arrhenius plot of ionic conductivity of the 2-QAFC and A201 membranes as a function of temperature. (c) Galvanostatic discharge of solid-state zinc–air batteries using the 2-QAFC, A201 and KOH-PC membranes at a current density of  $25 \text{ mA g}^{-1}$ . Inset shows an extended view of the red circle region at an initial 110 min. (d) Galvanostatic charge and discharge cycling of the 2-QAFC and A201 membranes at a current density of  $250 \text{ mA g}^{-1}$  with a 60 min per cycle period. (e) Galvanostatic charge and discharge cycling of the battery using pure oxygen and 20 000 ppm  $\text{CO}_2$  contaminated gas reactants, respectively, at a current density of  $250 \text{ mA g}^{-1}$  with a 60 min per cycle period, (f) corresponding Nyquist plots of the impedance of the battery at designated time segments. The inset of (e) showing an extended view of the first 420 min.

than that of the A201 membrane. The lower  $E_a$  suggests that the 2-QAFC membrane facilitates the hydroxide ion hopping in polymer chains compared to the A201 membrane as the temperature increases. It is likely that the nanoporous structure of the 2-QAFC membrane provides a significant amount of free volume, which leads to relatively high segmental motions of cellulose chains in the amorphous phase.

**Battery performance.** Compared to aqueous alkaline electrolytes in conventional zinc–air batteries, the hydration degree of solid-state electrolyte membranes is one of the key factors that influence the cell performance such as power output, capacity and cycle life. High water content of membranes can facilitate the conduction of hydroxide-ions and the resulting reaction kinetics of batteries. Additionally, a certain amount of residual water in membranes will be necessary to support sustained hydroxide-ion transport during battery operation because water also participates as the reactant in the oxygen reduction reaction during discharge. To construct a solid-state rechargeable zinc–air battery, we used commercial cobalt oxide nanoparticles loaded on a carbon cloth to prepare the bifunctional air electrode and paired it with a zinc electrode. The 2-QAFC membrane was

sandwiched between the two electrodes. The battery using the A201 membrane was also fabricated for comparison. Fig. 4c shows the galvanostatic discharge performance of the solid-state zinc-air battery using the 2-QAFC, A201 and KOH-PC (1 M KOH-doped pristine cellulose) membranes. The measurement was carried out at a constant current of  $25 \text{ mA g}^{-1}$  under atmospheric air. Although the A201 battery initially had a higher discharge voltage, the 2-QAFC battery quickly surpassed the A201 battery, showing a  $\sim 180 \text{ mV}$  higher voltage plateau and significantly higher discharge capacity (longer discharge time) after 25 min. While the KOH-PC battery shared a similar capacity with the 2-QAFC battery, the 2-QAFC battery displayed a higher discharge plateau, indicating a higher energy density of the 2-QAFC battery. The specific capacity of the battery using the 2-QAFC membrane normalized to the mass of zinc electrode was  $492 \text{ mA h g}^{-1}$ , which is superior to the values reported on solid-state Zn-air, Zn-MnO<sub>2</sub> and Li-ion batteries.<sup>6,49–51</sup> The battery as fabricated also showed a high power density of  $2362 \text{ mW g}^{-1}$  at a large current density of  $4650 \text{ mA g}^{-1}$  (Fig. S4, ESI†). The rapid voltage and capacity loss of the A201 membrane is due to a progressive loss of water and ionic conductivity in the membrane during the constant current discharge. It should be noted that simply wetting the A201 membrane by DDI water could regenerate the battery performance for subsequent runs with the same battery configuration. The gradual voltage decay of the battery using the KOH-PC membrane especially after 500 min is related to the continuous depletion of the alkali absorbed in the porous structure, which increased the overall resistance of the battery. On the other hand, the battery using the 2-QAFC membrane showed a steady decline from 1.3 V to 0.9 V after 500 min, and remained at this voltage over 1000 min. The steady performance can be attributed by the presence of high levels of bound water in the 2-QAFC membrane, thereby mitigating the ohmic polarization of the battery due to minimal loss of ionic conductivity. As a result, the 2-QAFC membrane exhibited a higher discharge capacity with a more stable voltage character in comparison to the commercial A201 membrane and the KOH-PC membrane.

**Cycle performance.** Fig. 4d further reveals the importance of the bound water in affecting the battery cycling performance. During discharge, the membrane shrinks as water is consumed by the oxygen reduction reaction. Meanwhile, the membrane may undergo stress and deformation from the volume expansion of the zinc electrode due to the formation of oxidized zinc species. During charge, the membrane is gradually swollen as water is generated for the oxygen evolution reaction. In addition, the internal pressure caused by the generated oxygen bubble and the formed zinc dendrite will lead to a mechanical failure of the membrane. To further verify the overall physical and ion-transport properties of the QAFC membranes, the galvanostatic charge and discharge cycling of the batteries using the 2-QAFC and A201 membranes were conducted. The battery was cycled at a high current of  $250 \text{ mA g}^{-1}$  with each cycle being 60 min (25% depth of discharge) under atmospheric air. Fig. 4d shows that the 2-QAFC membrane exhibited much longer cycle times with lower discharge and charge polarization than the commercial A201 membrane.

The battery using the A201 membrane deteriorated noticeably after 720 min, showing large discharge and charge polarizations, whereas the battery using the 2-QAFC membrane exhibited much better cycling stability without the loss of performance in both the charge and discharge over 2100 min. This superior cycling stability indicates that the 2-QAFC membrane, holding a larger amount of water as well as a smaller anisotropic swelling, can tolerate the periodic stress and dehydration during the discharge and charge process, and thus facilitates hydroxide-ion access to the electrodes. This assumption was confirmed by similarity in electrochemical impedance spectroscopy (EIS) results of the 2-QAFC battery in the duration of each 60 min-cycle segment, where no significant changes of the impedances were observed at designated intervals (10 min) for both the discharge and charge process, respectively (Fig. S5, ESI†). Additionally, the uninhibited hydroxide-ion availability to the electrodes is evident from a good reversibility of the zinc electrode during repeated cycles, where the absence of a compact passivation layer of oxidized zinc species on the zinc electrode surface was observed (Fig. S6, ESI†).

**Effect of CO<sub>2</sub>.** CO<sub>2</sub> contained in the air stream leads to the carbonation of the 2-QAFC membrane on reaction of the OH<sup>−</sup> with CO<sub>2</sub>. FTIR result (Fig. 2b) also reveals the presence of carbonate in the 2-QAFC membrane. The effect of CO<sub>2</sub> poisoning on the cycling performance of the 2-QAFC battery was investigated. The galvanostatic discharge and charge of the 2-QAFC battery were performed using pure oxygen as reference, and the oxygen gas containing 20 000 ppm CO<sub>2</sub>. The high CO<sub>2</sub> concentration ( $\sim 50$  times higher than that of air) in the mixture gas was used to enhance potential effects of the CO<sub>2</sub>. The 2-QAFC batteries were initially operated at an open-circle-voltage for two hours with flowing pure O<sub>2</sub> and 20 000 ppm CO<sub>2</sub> contaminated gas, respectively; then they were cycled under a current density of  $250 \text{ mA g}^{-1}$ . The galvanostatic cycling results under different gas conditions are shown in Fig. 4e. Compared to the pure O<sub>2</sub> condition, the initial higher polarization in the presence of CO<sub>2</sub> is likely related to increased ion (OH<sup>−</sup> and CO<sub>3</sub><sup>2−</sup>) transport resistances of the membrane. This effect correlates with the result that the membrane in CO<sub>3</sub><sup>2−</sup> form has a smaller conductivity compared to that of the membrane in OH<sup>−</sup> form (Table S1, ESI†). Interestingly, for the first 420 minutes, the battery polarization was progressively smaller with each passing cycle (Fig. 4e, inset). Additionally, after cycling over 420 min, only a slightly higher polarization was observed, compared to that of the battery cycled under pure O<sub>2</sub>. The results suggest that the residual carbonate content in the 2-QAFC membrane was decreasing, and thus, the observed similarity in battery performance between the case of pure O<sub>2</sub> and CO<sub>2</sub>/O<sub>2</sub> mixture after 420 min. It is possible that a high level of *in situ* “self-purging” process,<sup>52</sup> which has been previously reported in alkaline fuel cells, tends to occur at the air electrode, where OH<sup>−</sup> anions are continuously generated through the oxygen reduction reaction under high current densities. Additionally, the increased pH environment will be beneficial for the reaction kinetics, which further improves the battery performance. EIS results (Fig. 4f) reveal that the

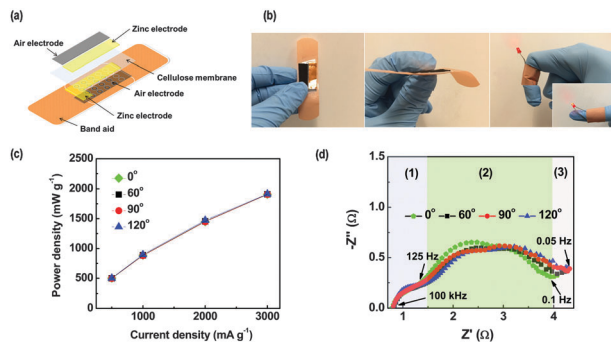


Fig. 5 (a) Schematic diagram of a flexible zinc–air battery device integrated with a band aid. (b) A demonstration of the flexible device wrapped around an index finger to power a red LED under bending condition. (c) Power densities of the single flexible cell as a function of current density at different bending angles. (d) Nyquist plots of the battery measured at a current density of 3000 mA g<sup>-1</sup> under different bending angles, within the frequency range from 0.05 Hz to 100 kHz.

charge-transfer resistance (polarization resistance) of the battery, in the present of CO<sub>2</sub>, decreased after 420 min (*i.e.*, 2010th min) compared to that at the initial stage (*i.e.*, 90th min). The drop in resistance, caused by continuous generation of OH<sup>-</sup> with self-purging, indicates an improvement of the charge-transfer kinetics and a decrease of the resultant battery polarization.

**Flexible device demonstration.** A flexible device using the 2-QAFC membrane was demonstrated for a simple proof-of-concept (Fig. 5a). Two flexible single cells (size 0.8 cm × 2.5 cm) were connected in series using a silver paste as an external circuit connection and fixed on the back side of a band aid. Here the band aid was used as a flexible and air-permeable substrate. As shown in Fig. 5b, the device as prepared was thin and flexible enough to be wrapped around a finger. Meanwhile, this device remained functional to power a red LED (light-emitting diode) when bent. To further understand the overall flexibility of the device, a single-cell device (size 1.0 cm × 2 cm) was fabricated onto a bendable nickel foam substrate to afford various bending conditions (Fig. S7, ESI<sup>†</sup>). Fig. 5c exhibits the output power density of the device as a function of current density under different angles. At any given angles, the power densities of the battery remained virtually unchanged under each different current density. Particularly, no significant power decay was detected even at an angle up to 120° at a high current density of 3000 mA g<sup>-1</sup>. The result indicates a robust physical property and high hydration level of the 2-QAFC membrane. The water can be held strongly by hydrogen bonds and capillary forces in hydrophilic nanopores of the 2-QAFC membrane, which does not restrict the hydroxide-ion conduction when the membrane was bended. The impedances of the 2-QAFC battery were further measured under atmospheric air within the frequency range from 0.05 Hz to 100 kHz. EIS spectra (Nyquist plots) of the 2-QAFC battery under various bending angles at a current density of 3000 mA g<sup>-1</sup> are presented in Fig. 5d. The battery resistance consists of three components: (1) a high-frequency incomplete arc mainly corresponds to OH<sup>-</sup> transport behaviour ( $R_{int}$ ) at the interface of the membrane and electrodes;

(2) a medium-frequency semicircle represents a charge-transfer resistance ( $R_{ct}$ ) in parallel to the electrode double layer capacitance; (3) a low-frequency tail is attributed to the mass transport limitations of reactants (*i.e.*, oxygen, water, zinc species). The values of  $R_{int}$  exhibited minuscule changes even bending towards large angles (Table S2, ESI<sup>†</sup>), indicating uninhibited OH<sup>-</sup> transport process between the membrane and the electrodes. Additionally, the  $R_{ct}$  values did not show significant variation with changes in bending angles (Table S2, ESI<sup>†</sup>), which again reveals that the 2-QAFC membrane possesses high flexibility to precede the oxygen reduction reaction by strongly holding a large amount of water within its nanofibrous structure.

## Conclusions

In summary, for the first time, a highly flexible and hydroxide conductive porous electrolyte membrane, made of the functionalized cellulose nanofibres, was fabricated and utilized as both a solid electrolyte and a separator for rechargeable, solid-state zinc–air battery applications. The superior hydroxide-ion conductive property and water retention within the nanoporous structure of the membrane as well as low anisotropic swelling boosted the specific capacity and improved the cycling stability of the battery, compared to the commercial alkaline anion-exchange membrane (A201). A flexible zinc–air battery device was created and further demonstrated the outstanding electrochemical and mechanical performance of the membrane, where virtually no power density fading nor polarization of the battery were observed for the discharge and the charge process under bending conditions. Therefore, this novel concept of using natural cellulose nanofibres to prepare the hydroxide-conductive solid-state electrolyte with high water retention will open up a new possibility for the development of high-performance, flexible, environmentally-friendly and cost-effective rechargeable zinc–air batteries.

## Acknowledgements

This research was supported by the Natural Sciences and Engineering Research Council of Canada (NSERC). The authors would like to thank Professor Bo Cui at the University of Waterloo for providing support with AFM analysis.

## Notes and references

- 1 L. Li, Z. Wu, S. Yuan and X.-B. Zhang, *Energy Environ. Sci.*, 2014, **7**, 2101–2122.
- 2 G. Nystrom, A. Marais, E. Karabulut, L. Wagberg, Y. Cui and M. M. Hamed, *Nat. Commun.*, 2015, **6**, 7259.
- 3 M. H. Park, M. Noh, S. Lee, M. Ko, S. Chae, S. Sim, S. Choi, H. Kim, H. Nam, S. Park and J. Cho, *Nano Lett.*, 2014, **14**, 4083–4089.
- 4 Y. Sun, R. B. Sills, X. Hu, Z. W. Seh, X. Xiao, H. Xu, W. Luo, H. Jin, Y. Xin, T. Li, Z. Zhang, J. Zhou, W. Cai, Y. Huang and Y. Cui, *Nano Lett.*, 2015, **15**, 3899–3906.
- 5 M. Winter and R. J. Brodd, *Chem. Rev.*, 2004, **104**, 4245–4270.

- 6 J. Fu, D. U. Lee, F. M. Hassan, L. Yang, Z. Bai, M. G. Park and Z. Chen, *Adv. Mater.*, 2015, **27**, 5617–5622.
- 7 J. Park, M. Park, G. Nam, J.-s. Lee and J. Cho, *Adv. Mater.*, 2015, **27**, 1396–1401.
- 8 J. S. Lee, S. Tai Kim, R. Cao, N.-S. Choi, M. Liu, K. T. Lee and J. Cho, *Adv. Energy Mater.*, 2011, **1**, 34–50.
- 9 Y. Li and H. Dai, *Chem. Soc. Rev.*, 2014, **43**, 5257–5275.
- 10 Y. Li, M. Gong, Y. Liang, J. Feng, J.-E. Kim, H. Wang, G. Hong, B. Zhang and H. Dai, *Nat. Commun.*, 2013, **4**, 1805.
- 11 D. U. Lee, J. Y. Choi, K. Feng, H. W. Park and Z. Chen, *Adv. Energy Mater.*, 2014, **4**, 130189.
- 12 D. U. Lee, B. J. Kim and Z. Chen, *J. Mater. Chem. A*, 2013, **1**, 4754–4762.
- 13 D. U. Lee, H. W. Park, M. G. Park, V. Ismayilov and Z. Chen, *ACS Appl. Mater. Interfaces*, 2015, **7**, 902–910.
- 14 X. Liu, M. Park, M. G. Kim, S. Gupta, G. Wu and J. Cho, *Angew. Chem., Int. Ed.*, 2015, **54**, 9654–9658.
- 15 Y. J. Wang, J. Qiao, R. Baker and J. Zhang, *Chem. Soc. Rev.*, 2013, **42**, 5768–5787.
- 16 S. Gu, J. Wang, R. B. Kaspar, Q. Fang, B. Zhang, E. Bryan Coughlin and Y. Yan, *Sci. Rep.*, 2015, **5**, 11668.
- 17 H. Zarrin, J. Wu, M. Fowler and Z. Chen, *J. Membr. Sci.*, 2012, **394–395**, 193–201.
- 18 S. Gu, R. Cai and Y. Yan, *Chem. Commun.*, 2011, **47**, 2856–2858.
- 19 S. Gu, R. Cai, T. Luo, Z. Chen, M. Sun, Y. Liu, G. He and Y. Yan, *Angew. Chem., Int. Ed.*, 2009, **48**, 6499–6502.
- 20 Z. Gui, H. Zhu, E. Gillette, X. Han, G. W. Rubloff, L. Hu and S. B. Lee, *ACS Nano*, 2013, **7**, 6037–6046.
- 21 H. Zhu, Z. Xiao, D. Liu, Y. Li, N. J. Weadock, Z. Fang, J. Huang and L. Hu, *Energy Environ. Sci.*, 2013, **6**, 2105–2111.
- 22 H. Zhu, Z. Fang, C. Preston, Y. Li and L. Hu, *Energy Environ. Sci.*, 2014, **7**, 269–287.
- 23 G. Zheng, Y. Cui, E. Karabulut, L. Wågberg, H. Zhu and L. Hu, *MRS Bull.*, 2013, **38**, 320–325.
- 24 G. Zhou, F. Li and H.-M. Cheng, *Energy Environ. Sci.*, 2014, **7**, 1307–1338.
- 25 X. Lu, M. Yu, G. Wang, Y. Tong and Y. Li, *Energy Environ. Sci.*, 2014, **7**, 2160–2181.
- 26 L. Hu and Y. Cui, *Energy Environ. Sci.*, 2012, **5**, 6423–6435.
- 27 Z. Fang, H. Zhu, W. Bao, C. Preston, Z. Liu, J. Dai, Y. Li and L. Hu, *Energy Environ. Sci.*, 2014, **7**, 3313–3319.
- 28 L. Hu, G. Zheng, J. Yao, N. Liu, B. Weil, M. Eskilsson, E. Karabulut, Z. Ruan, S. Fan, J. T. Bloking, M. D. McGehee, L. Wågberg and Y. Cui, *Energy Environ. Sci.*, 2013, **6**, 513–518.
- 29 H. Wei, K. Rodriguez, S. Renneckar and P. J. Vikesland, *Environ. Sci.: Nano*, 2014, **1**, 302–316.
- 30 M. Andresen, P. Stenstad, T. Møretro, S. Langsrud, K. Syverud, L.-S. Johansson and P. Stenius, *Biomacromolecules*, 2007, **8**, 2149–2155.
- 31 S. Yun, K. S. Kang and J. Kim, *Polym. Int.*, 2010, **59**, 1071–1076.
- 32 Y. Zhao, R. Nakamura, K. Kamiya, S. Nakanishi and K. Hashimoto, *Nat. Commun.*, 2013, **4**, 2390.
- 33 S. Gu, J. Skovgard and Y. S. Yan, *ChemSusChem*, 2012, **5**, 843–848.
- 34 S. Park, J. Baker, M. Himmel, P. Parilla and D. Johnson, *Biotechnol. Biofuels*, 2010, **3**, 1–10.
- 35 Q. Duan, S. Ge and C.-Y. Wang, *J. Power Sources*, 2013, **243**, 773–778.
- 36 S. P. Mishra, *A Text Book of Fibre Science and Technology*, New Age International, 2000.
- 37 Y.-S. Park and Y. Yamazaki, *J. Membr. Sci.*, 2005, **261**, 58–66.
- 38 A. M. Kiss, T. D. Myles, K. N. Grew, A. A. Peracchio, G. J. Nelson and W. K. S. Chiu, *J. Electrochem. Soc.*, 2013, **160**, F994–F999.
- 39 J. Lu, P. Askeland and L. T. Drzal, *Polymer*, 2008, **49**, 1285–1296.
- 40 B. Kumar, M. Asadi, D. Pisasale, S. Sinha-Ray, B. A. Rosen, R. Haasch, J. Abiade, A. L. Yarin and A. Salehi-Khojin, *Nat. Commun.*, 2013, **4**, 2819.
- 41 Z. Fang, H. Zhu, Y. Yuan, D. Ha, S. Zhu, C. Preston, Q. Chen, Y. Li, X. Han, S. Lee, G. Chen, T. Li, J. Munday, J. Huang and L. Hu, *Nano Lett.*, 2014, **14**, 765–773.
- 42 C. Hu, J. Zhu and K. Li, *Holzforchung*, 2015, **69**, 993–1000.
- 43 F. Jianhua and G. Xiaoxia, *Electrochemical Polymer Electrolyte Membranes*, CRC Press, 2015, pp. 315–364.
- 44 J. Fu, J. Qiao, H. Lv, J. Ma, X.-Z. Yuan and H. Wang, *ECS Trans.*, 2010, **25**, 15–23.
- 45 J. Qiao, J. Fu, L. Liu, Y. Liu and J. Sheng, *Int. J. Hydrogen Energy*, 2012, **37**, 4580–4589.
- 46 J. Qiao, J. Fu, R. Lin, J. Ma and J. Liu, *Polymer*, 2010, **51**, 4850–4859.
- 47 H. Gao and K. Lian, *RSC Adv.*, 2014, **4**, 33091–33113.
- 48 X. Ren, S. C. Price, A. C. Jackson, N. Pomerantz and F. L. Beyer, *ACS Appl. Mater. Interfaces*, 2014, **6**, 13330–13333.
- 49 Z. Wang, Z. Wu, N. Bramnik and S. Mitra, *Adv. Mater.*, 2014, **26**, 970–976.
- 50 Q. Cheng, Z. Song, T. Ma, B. B. Smith, R. Tang, H. Yu, H. Jiang and C. K. Chan, *Nano Lett.*, 2013, **13**, 4969–4974.
- 51 Y. Xu, Y. Zhang, Z. Guo, J. Ren, Y. Wang and H. Peng, *Angew. Chem., Int. Ed.*, 2015, **54**, 15390–15394.
- 52 L. A. Adams, S. D. Poynton, C. Tamain, R. C. T. Slade and J. R. Varcoe, *ChemSusChem*, 2008, **1**, 79–81.